AGU PUBLICATIONS

Geophysical Research Letters

RESEARCH LETTER
10.1002/2014GL060523

Key Points:
- Lunar crustal fields decelerate and reflect solar wind protons and alphas
- Crustal fields suppress local sputtering rates for the exosphere
- Exospheric distributions for sputtered species can be highly anisotropic

Correspondence to:
A. R. Poppe,
poppe@ssl.berkeley.edu

Citation:
Poppe, A. R., M. Sarantos, J. S. Halekas, G. T. Delory, Y. Saito, and M. Nishino (2014), Anisotropic solar wind sputtering of the lunar surface induced by crustal magnetic anomalies, *Geophys. Res. Lett.*, *41*, doi:10.1002/2014GL060523.

Received 13 MAY 2014
Accepted 3 JUL 2014
Accepted article online 9 JUL 2014

Anisotropic solar wind sputtering of the lunar surface induced by crustal magnetic anomalies

A. R. Poppe[1,2], M. Sarantos[2,3,4], J. S. Halekas[1,2], G. T. Delory[1,2], Y. Saito[5], and M. Nishino[6]

[1]Space Sciences Laboratory, University of California, Berkeley, California, USA, [2]Solar System Exploration Research Virtual Institute, NASA Ames Research Center, Mountain View, California, USA, [3]Goddard Planetary Heliophysics Institute, University of Maryland, Baltimore County, Baltimore, Maryland, USA, [4]NASA Goddard Space Flight Center, Greenbelt, Maryland, USA, [5]Institute of Space and Astronautical Science, Japan Aerospace Exploration Agency, Tokyo, Japan, [6]Solar-Terrestrial Environment Laboratory, Nagoya University, Nagoya, Japan

Abstract The lunar exosphere is generated by several processes each of which generates neutral distributions with different spatial and temporal variability. Solar wind sputtering of the lunar surface is a major process for many regolith-derived species and typically generates neutral distributions with a cosine dependence on solar zenith angle. Complicating this picture are remanent crustal magnetic anomalies on the lunar surface, which decelerate and partially reflect the solar wind before it strikes the surface. We use Kaguya maps of solar wind reflection efficiencies, Lunar Prospector maps of crustal field strengths, and published neutral sputtering yields to calculate anisotropic solar wind sputtering maps. We feed these maps to a Monte Carlo neutral exospheric model to explore three-dimensional exospheric anisotropies and find that significant anisotropies should be present in the neutral exosphere depending on selenographic location and solar wind conditions. Better understanding of solar wind/crustal anomaly interactions could potentially improve our results.

1. Introduction

The lunar exosphere is a tenuous, collisionless collection of neutrals generated through a variety of processes, including sputtering by incident charged particles such as the solar wind or terrestrial plasma sheet [*Johnson and Baragiola*, 1991; *Wurz et al.*, 2007]. Upon striking the lunar surface regolith, high-energy (≈0.5–5 keV) solar wind protons and alphas (doubly charged helium) eject neutral atoms from individual grains with a composition reflecting that of the regolith itself, producing a significant fraction of neutral exospheric column density for species such as O, Si, Fe, Ca, Mg, Al, and Ti [*Wurz et al.*, 2007; *Sarantos et al.*, 2012b; *Vorburger et al.*, 2014]. Due to the nature of the incident solar wind flux, the spatial distribution of the sputtered neutral flux from the surface is typically assumed to be proportional to $\cos\alpha$, where α is the solar zenith angle, similar to that observed in reflected energetic neutral atoms (ENAs) [*Wieser et al.*, 2009; *Schaufelberger et al.*, 2011]; however, studies to date have not yet considered the effect that crustal magnetic anomalies may have on altering the solar wind flux and resulting sputtered exospheric neutral distributions.

Several spacecraft have observed solar wind proton reflection from both the lunar surface and remanent crustal magnetic fields, including Nozomi [*Futaana et al.*, 2003], Kaguya [*Saito et al.*, 2008, 2012], Chandrayaan-1 [*Lue et al.*, 2011], Chang'e 1 [*Wang et al.*, 2010], and ARTEMIS [*Halekas et al.*, 2013b]. Energetic neutral atom (ENA) observations have also demonstrated local suppressions in backscattered ENA flux in regions with crustal magnetic anomalies [*Wieser et al.*, 2010; *Vorburger et al.*, 2012; *Futaana et al.*, 2013]. These observations show that solar wind protons are scattered from nonmagnetized regions of the lunar surface with an average efficiency of 0.1–1% [*Saito et al.*, 2008] and from crustal anomalies with regionally averaged efficiencies of ≈10% and local enhancements (due to very strong crustal anomalies) up to almost 90% [*Lue et al.*, 2011]. Observations, laboratory experiments, and models have suggested that the primary mechanisms by which protons are reflected include both nonadiabatic scattering by the crustal magnetic fields and the formation of electrostatic fields due to decoupling between electrons and protons as they enter the anomaly region [*Saito et al.*, 2012; *Bamford et al.*, 2012; *Poppe et al.*, 2012; *Wang et al.*, 2013; *Futaana et al.*, 2013; *Deca et al.*, 2014; *Jarvinen et al.*, 2014]. Observations also suggest that some fraction of solar wind ions incident on crustal magnetic anomalies are deflected laterally yet still strike the surface [*Vorburger et al.*, 2012]. The deceleration and reflection of solar wind protons by electrostatic fields

associated with lunar crustal magnetic anomalies decreases both the incident solar wind flux and the resulting neutral sputtered flux in the area occupied by each anomaly. Thus, regions above crustal magnetic anomalies may have lower neutral exospheric densities for surface-sputtered species, an important conclusion given both recently reported measurements of neutral sputtered oxygen [*Vorburger et al.*, 2014] and ongoing measurements and analysis of exospheric observations by the Lunar Atmospheric and Dust Environment Explorer (LADEE) mission.

In this paper, we calculate anisotropies in solar wind sputtered neutral distributions that occur due to the deceleration and reflection of solar wind protons by crustal magnetic anomalies. In section 2, we describe our calculations of anisotropic solar wind flux and sputtering rates on the lunar surface and present results for two example solar wind conditions. In section 3, we use the maps of sputtering rates in a neutral exospheric model to investigate the resulting anisotropies in the lunar exosphere. Finally, we discuss implications for in situ measurements of sputtered neutral exospheric species and conclude in section 4.

2. Crustal Anomaly Impacts on Sputtering

Figure 1a shows the fraction of reflected solar wind proton flux as observed by the Kaguya mission as a function of selenographic longitude and latitude. The regions of greatest reflected flux correspond to the known locations of crustal magnetic anomalies, whose strength at the surface is shown in Figure 1b as measured by the Lunar Prospector Electron Reflectometer [*Mitchell et al.*, 2008]. In the southern hemisphere near 180° longitude, the South Pole-Aitken Basin region contains both the strongest and largest collection of crustal fields, with smaller and weaker fields across much of the rest of the lunar surface. We subtracted off the fraction of solar wind protons that scatter in charged form from the lunar regolith across the entire surface (≈1%) as these protons are not reflected by crustal anomaly-induced electrostatic fields [*Saito et al.*, 2008]; notably, this correction is much smaller than the fractional flux typically reflected by crustal magnetic fields.

In addition to observing the global flux of reflected protons, the Kaguya mission has also reported measurements of the likely mechanism by which these protons are reflected [*Saito et al.*, 2012]. Briefly, as solar wind protons and electrons approach a magnetic anomaly, the magnetized electrons are reflected by the magnetic fields via magnetic mirroring, while the protons, whose gyroradii are too large to be magnetized, penetrate deeper into the anomaly. The ensuing charge separation between the electrons and ions sets up an electric field that decelerates the protons and if strong enough, either deflects or completely reflects protons from the anomaly region before they strike the surface. Such electrostatic fields have been inferred by the Kaguya mission over crustal anomalies [*Saito et al.*, 2012] and ENA measurements by Chandrayaan [*Futaana et al.*, 2013], observed in laboratory settings [*Bamford et al.*, 2012; *Wang et al.*, 2012], and seen in plasma simulations [*Poppe et al.*, 2012; *Deca et al.*, 2014; *Jarvinen et al.*, 2014]. As observed by Kaguya, the presence of electrostatic fields above crustal magnetic fields can decelerate the entire solar wind proton distribution and reflect up to approximately 35% of the solar wind proton flux at specific locations. Importantly, we note that solar wind alpha particles will also be decelerated by magnetic anomaly-induced electrostatic potentials. Solar wind alpha fractions in the solar wind typically range between 1 and 5% (although excursions up to 20–25% have been reported); however, given their higher mass, alpha particles are more efficient sputterers than protons [*Biersack and Eckstein*, 1984; *Johnson and Baragiola*, 1991] and their contribution to the total neutral sputtered flux is typically around 20–30% [*Wurz et al.*, 2007]. Highly charged, heavy ions in the solar wind may also contribute to sputtering, both kinetically due to their higher mass and via potential sputtering due to the typically high charge state of these ions [*Meyer et al.*, 2011; *Barghouty et al.*, 2011]. *Wurz et al.* [2007] dismissed the potential sputtering contribution due to a fluence effect whereby the oxide surface is preferentially depleted of oxygen and becomes relatively conducting, which neutralizes the effect of potential sputtering; however, *Meyer et al.* [2011] observed no such effect using lunar simulant material. Given the uncertainty in the applicability of potential sputtering of the lunar surface, we do not include any contribution of highly charged, heavy ions at this time.

In order to estimate the solar wind velocity distribution at the lunar surface within regions with crustal magnetic fields, we must first estimate the magnitude of electrostatic potentials induced by crustal magnetic anomalies at each location. We estimated the strength of these potentials by using two complementary methods: (1) calculating the electrostatic potential required to reflect a given fraction of the solar wind flux as observed by Kaguya and (2) using results from particle-in-cell simulations of solar wind/crustal magnetic anomaly interactions [*Poppe et al.*, 2012]. For method (1), we assume that the entire flux of reflected protons

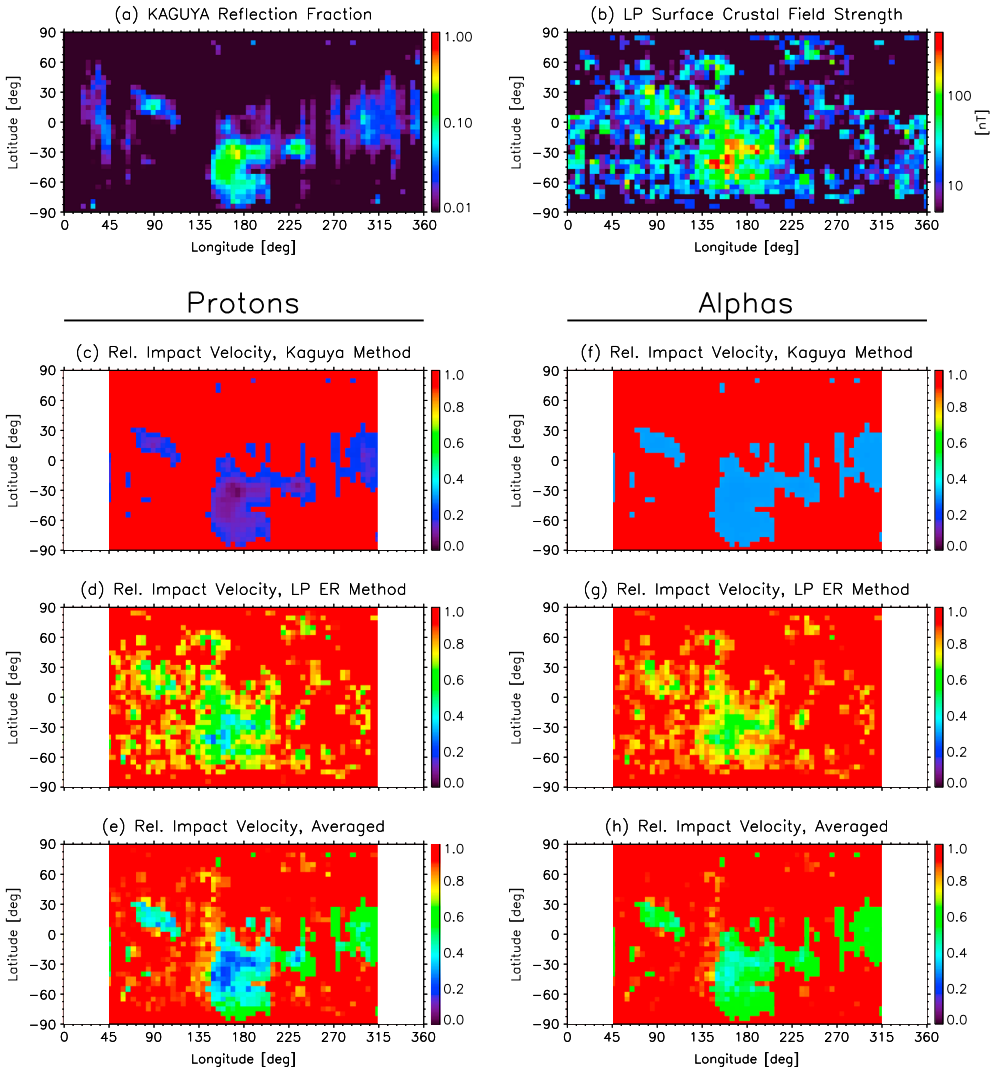

Figure 1. (a) The average fraction of reflected proton flux from lunar crustal magnetic anomalies as observed by the Kaguya mission. The longitude is oriented such that the South Pole-Aitken Basin is centered at approximately 180°. (b) The surface magnetic field as measured by the Lunar Prospector Electron Reflectometer, binned at 5 × 5° resolution, with a maximum value at ≈ 250 nT [*Mitchell et al.*, 2008]. For protons: (c) the relative solar wind velocity at the lunar surface derived from the Kaguya reflection maps as described in the text [*Saito et al.*, 2012], (d) the relative solar wind velocity at the lunar surface derived from Lunar Prospector Electron Reflectometer (LP ER) data as described in the text, and (e) the relative solar wind velocity at the lunar surface averaged between the two methods. (f–h) The same quantities for alphas. White regions indicate portions of the lunar surface not typically exposed to direct solar wind flow.

observed by Kaguya was due to electrostatic reflection. We note that nonadiabatic magnetic scattering by the crustal fields may also contribute to reflecting protons; however, we do not include such an effect in our estimation at this time as recent work has suggested that this is secondary to electrostatic reflection [*Bamford et al.*, 2012; *Deca et al.*, 2014]. We calculate the electrostatic potential necessary to reflect a given fraction of solar wind flux by decelerating the proton distribution in velocity space until the given amount of proton flux is reflected. Figure 1c shows the relative solar wind velocity at the lunar surface as calculated by this method, demonstrating that in areas with observed proton reflection, the solar wind distribution must be significantly slowed ($\approx 0.2\ v_{sw}$) by the time it reaches the surface.

Importantly, method (1) only estimates electrostatic potentials in regions where Kaguya has observed reflected flux; however, somewhat weaker crustal fields may also partially decelerate, yet not reflect, the solar wind before it impacts the surface and we must account for this. Thus, method (2) uses the Lunar Prospector maps of surface crustal magnetic field strength [*Mitchell et al.*, 2008] and particle-in-cell (PIC)

modeling results [*Poppe et al.*, 2012] to estimate the strength of the electrostatic potential given the surface magnetic field strength, Figure 1d. We note that while these PIC modeling results are only strictly valid for cusp regions of magnetic anomalies, they have been favorably compared with Kaguya observations [*Saito et al.*, 2012] and provide at least a first-order estimate. Higher-dimensional simulations using more realistic crustal magnetic field geometries may provide a better estimate of the strength of these potentials. We find good qualitative agreement between the two methods in regions strong enough to reflect flux, allowing for the anticipated differences in the two methods as described above. Some regions of Kaguya reflected flux do not obviously line up with known crustal field regions, although this may be due to the presence of short-wavelength, small-scale crustal magnetic anomalies on the lunar surface, which are typically underestimated in strength by electron reflectometry yet may still serve to efficiently reflect the solar wind [*Halekas et al.*, 2010]. Thus, to compile a final map of electrostatic potential, we take the average calculated potential at each location from both methods and calculate the bulk solar wind velocity at the lunar surface for each selenographic location, shown in Figure 1e, where we have masked out regions of the lunar surface that are never directly exposed to the solar wind (i.e., lunar nearside). In regions with no crustal fields, solar wind protons impact the surface at their full velocity, while in regions with crustal fields, protons can be decelerated down to ≈20% of their unperturbed speed. We repeat this calculation for the alphas (which are decelerated less), shown in Figures 1f–1h, and thus, at each location on the lunar surface, calculate the impacting solar wind proton and alpha distributions by decelerating each unperturbed distribution, initially assumed as a cold, drifting Maxwellian, through the estimated electrostatic potential.

We note that solar wind protons reflected from magnetic anomalies may be placed on trajectories that cause them to reimpact the lunar surface at another location. We conducted extensive particle tracing of such protons and found that reimpacting protons contributed only a very small fraction of flux relative to the original solar wind (< 1%); therefore, we neglect this contribution. We also note that observations [*Lue et al.*, 2011; *Saito et al.*, 2012] and simulations [*Poppe et al.*, 2012] have suggested that the solar wind beam may be heated (either kinetically through ion-ion instabilities, effectively through nonadiabatic magnetic scattering, or via other processes) within the anomaly region before striking the surface. Such a process would to some degree restore the level of sputtering flux within anomaly regions; however, given the present uncertainty in the existence and nature of this heating, we do not include this effect in our calculations. A deeper understanding of the microphysics deep within crustal anomaly interaction regions may allow us to further refine these calculations in the future.

Using the solar wind deceleration velocity calculated above, the sputtered neutral flux at each location, $\Gamma_s(\phi, \theta)$, where ϕ and θ are the subsolar longitude and latitude, respectively, can be determined by integrating the impacting particle distribution, $f'_s(E, \phi, \theta)$, where the prime indicates the distribution after deceleration, s refers to the species, protons, or alphas, and the distribution for each is a drifting Maxwellian with a typical temperature, $T_i = 10$ eV, with the sputtering yield, $Y_s(E)$, via:

$$\Gamma_s(\phi, \theta) = \int Y_s(E) f'_s(E, \phi, \theta) \cos\alpha \mathrm{d}E, \quad (1)$$

where we have also included a $\cos\alpha$ factor to account for the cosine solar zenith angle nature of the unperturbed solar wind flux. The sputtering yields as a function of energy are taken from Transport of Ions in Materials: Sputtering version (TRIM.SP) modeling results, which show peaks in the sputtering yields at impact energies of approximately 1 keV for both protons and alphas with a steep decline in yield for energies below approximately 100 eV [*Biersack and Eckstein*, 1984, Figure 17]. The sharp decline in sputtering yields for low energies ($E < 100$ eV) implies that crustal magnetic anomalies do not necessarily need to entirely reflect the solar wind to completely suppress local sputtering; rather, they need only decelerate the bulk of the solar wind distribution below 100 eV, at which point the proton and alpha sputtering yields drop to zero. Even partial deceleration of the solar wind will induce a decline in local sputtered fluxes as part of the solar wind distribution falls below the minimum sputtering energy of approximately 100 eV. Figure 2 illustrates this by showing the average sputtering yield as a function of impact velocity for both protons and alphas, where we integrated over a convolution of the sputtering yield and particle energy distributions (assuming a temperature, shown in Figure 2). For typical solar wind impact velocities (≈ 250–650 km/s), the yields for protons and alphas are approximately 0.01 and 0.1, respectively. As each distribution is slowed, both curves rise slightly as the particle distribution passes through the peak yield before declining. The proton sputtering yield diminishes faster as a function of energy than the alpha yield, and thus, for very low velocities the ratio of alpha to proton sputtering yields

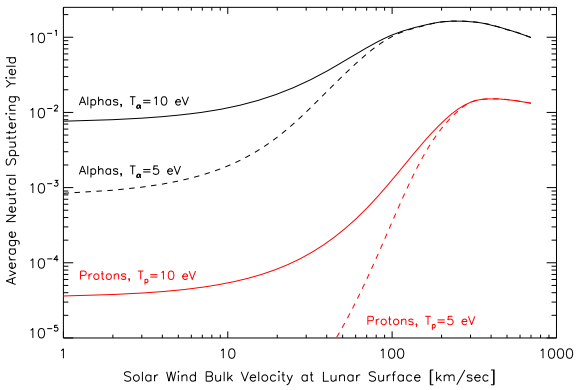

Figure 2. The average neutral sputtering yield for incident solar wind protons and alphas as a function of bulk velocity at the lunar surface. Solid and dashed lines are for particle temperatures of 10 and 5 eV, respectively.

is greater than 100. The temperature of each distribution also plays a role in altering the effective sputtering yields at low velocities, as colder temperatures confine more of each distribution to energies below the cutoff in each species respective sputtering yield as each distribution is decelerated.

Combining the solar wind flux to each point on the lunar surface and the neutral sputtering yields, we can calculate a global map of the relative neutral sputtered flux for protons, alphas, and their sum, shown in Figure 3 at new Moon (South Pole/Aitken Basin at local noon) for two different solar wind cases: $v_{sw} = 250$ km/s with a 1% alpha content and $v_{sw} = 450$ km/s with a 5% alpha content. In the first case, the sputtered fluxes for both protons and alphas are significantly diminished in regions where crustal fields are present, mainly in the southern hemisphere. Proton-sputtered fluxes drop more than an order of magnitude relative to that expected when crustal fields are not taken into account. The solar wind alpha-sputtered flux also shows a relative depression at approximately 50% of maximum in the same crustal field regions, given that the electrostatic potentials above crustal anomalies decelerate alphas less given their lower charge-to-mass ratio. Figure 3c shows the weighted sum (99% protons, 1% alphas for this case) of the sputtered fluxes, with a net relative decrease in the sputtered flux still greater than 1 order of magnitude.

Figures 3d–3f show the second solar wind case: $v_{sw} = 450$ km/s with a 5% alpha content. The protons behave similarly to the 250 km/s case, with slightly more sputtering in the crustal field regions but still more than an order of magnitude decrease. The alphas, in contrast, show an increase in the sputtered yield over the crustal anomaly regions. Inspection of Figure 2 shows that the alpha sputtering yields reach a maximum at approximately 250 km/s, and thus, alphas slowed from an undisturbed velocity of 450 km/s will initially increase their effective sputtering yield before declining for speeds less than 250 km/s. In fact, the effective proton sputtering yield shows a similar effect with a maximum at approximately 400 km/s; however, the electrostatic fields above crustal anomalies typically decelerate protons much below 400 km/s where the sputtering yield quickly diminishes. Overall, Figure 3f shows the net sputtered flux from both protons and alphas at each geographical location for this case and despite the relative increase in the alpha-sputtered flux component, the total sputtered flux is still depressed in the southern hemisphere by more than 50%.

3. Sputtered Neutral Exospheric Modeling

In order to characterize the effect that crustal field suppression of solar wind sputtering has on the global structure and distribution of the lunar exosphere, we have integrated maps of the relative sputtered flux shown in Figure 3 into a Monte Carlo variant of the neutral exospheric model described in *Sarantos et al.* [2012b]. This model launches 1 million test particles from the dayside lunar surface and propagates them in the lunar gravitational field to calculate the density of neutrals at any point above the surface given the initial ejection velocity distribution, a Sigmund-Thomson for sputtered neutrals [*Thompson et al.*, 1968; *Sigmund*, 1969; *Husinsky et al.*, 1985], and the surface source rate, i.e., Figure 3. Initial velocities are distributed with a distribution relative to the local surface normal as, $f(\alpha) \propto \cos\alpha$, as expected for sputtering from a porous regolith [*Cassidy and Johnson*, 2005]. Figure 4 shows the resulting neutral sputtered oxygen distribution in two planar slices, (a) *X-Z* and (b) *X-Y*, for solar wind conditions, $v_{sw} = 250$ km/s and $\alpha/p = 0.01$, corresponding to the surface map shown in Figure 3c. In both planes, the effect of crustal field suppression of sputtered flux is readily apparent at low altitudes. For the lunar phase modeled (new Moon), the northern hemisphere has very little crustal magnetism and the sputtered exospheric distribution resembles the standard $\cos\alpha$ exosphere, while in the southern hemisphere, the suppression of sputtering by the South Pole-Aitken Basin crustal anomalies results in nearly an order of magnitude decrease in neutral density. In the equatorial plane, Figure 4b, the neutral exospheric distribution is highly structured at low altitudes as individual anomalies locally suppress the sputtering rate. In both planes, the exospheric neutral

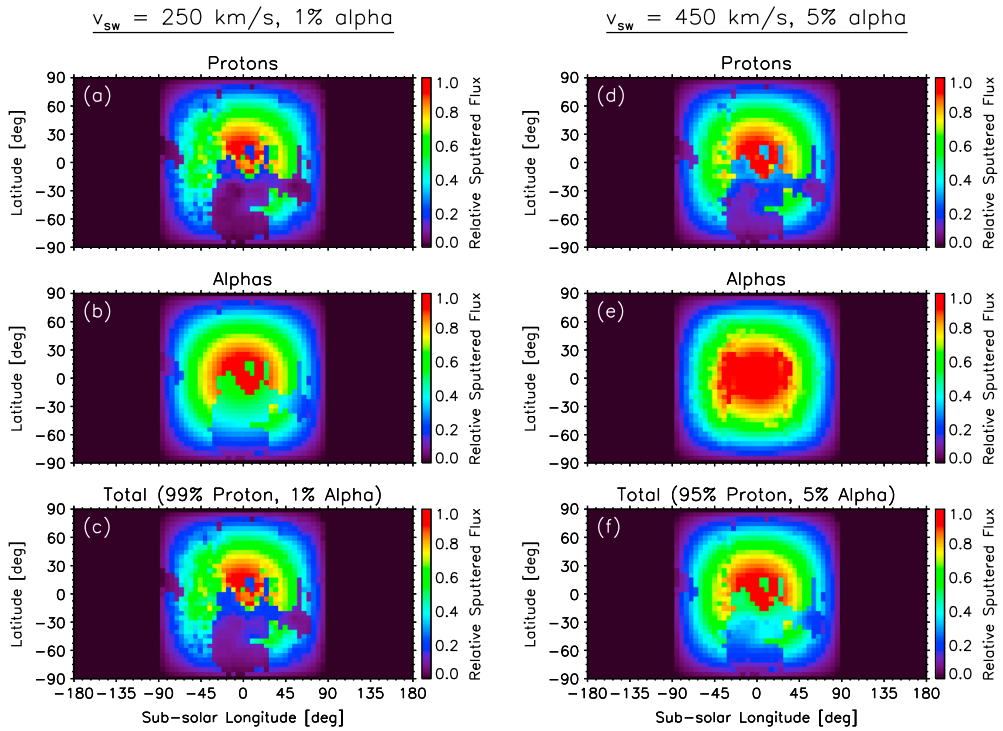

Figure 3. Subsolar centered maps at new Moon of the relative sputtered flux of neutrals taking into account the effect of crustal magnetic anomaly deceleration and shielding of the lunar surface. (a) Proton, (b) alpha, and (c) total maps for v_{sw} = 250 km/s and 1% alpha content. (d–f) Same as Figures 3a–3c but for v_{sw} = 450 km/s, 5% alpha content. Each individual panel is normalized to the maximum sputtered flux expected for that species in the absence of crustal field effects.

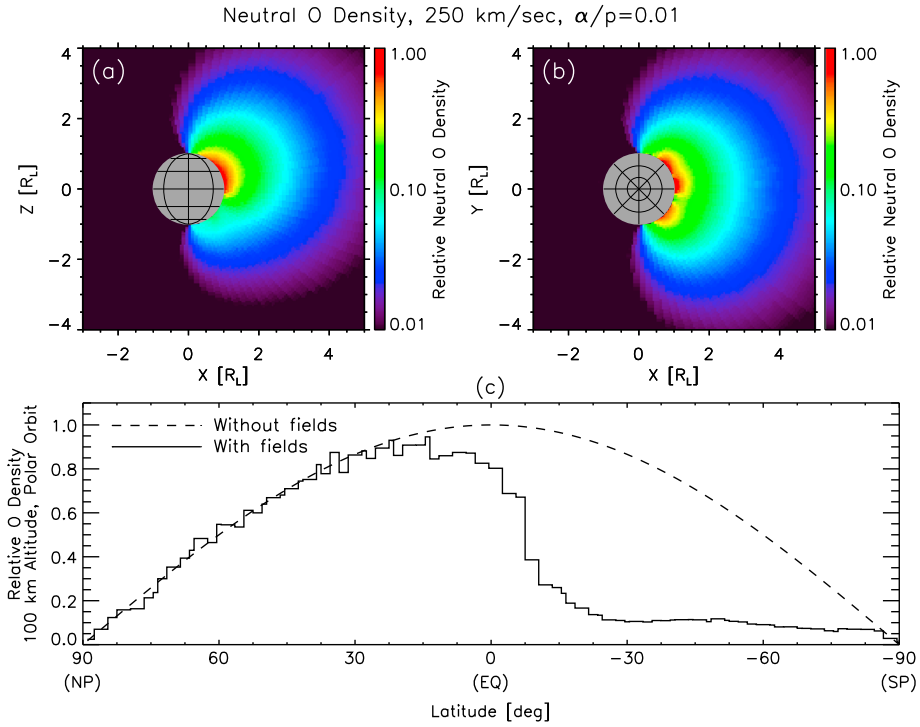

Figure 4. A two-dimensional slice through the relative neutral sputtered oxygen density in (a) the *X-Z* plane and (b) the *X-Y* plane for v_{sw} = 250 km/s, α/p = 0.01 at new Moon. (c) The relative sputtered neutral oxygen density along a 100 km altitude polar orbit as a function of latitude both with and without the effect of crustal field suppression of sputtering. "NP," "EQ," and "SP" denote the north pole, equator, and south pole, respectively.

distribution at high altitudes more closely resembles the cos α distribution expected for uniform sputtering, although we do note that some anisotropy is still observable at altitudes exceeding one lunar radii in the southern hemisphere, Figure 4 a, for example. Finally, Figure 4c shows the relative sputtered neutral oxygen density along a polar, 100 km altitude orbit compared to simulations with and without the effect of crustal fields. Neutral densities in the northern hemisphere closely match that expected from the isotropic sputtering model, while densities in the southern hemisphere are strongly suppressed.

4. Conclusion

We have used a combination of Kaguya observations of reflected protons, Lunar Prospector maps of remanent crustal magnetic field strength, neutral sputtering yields, and an exospheric model to characterize anisotropies in the solar wind sputtered component of the lunar neutral exosphere due to the electromagnetic interaction of lunar crustal fields with the ambient solar wind. The observed deceleration and partial reflection of solar wind protons and alphas over crustal magnetic field regions implies that neutral sputtered fluxes are suppressed in these regions. In turn, the sputtered component of the lunar neutral exosphere contains anisotropies that may be observable by spacecraft instrumentation, including both the Energetic Neutral Analyzer onboard the Chandrayaan spacecraft, which has recently reported neutral sputtered oxygen observations [*Vorburger et al.*, 2014], and the Lunar Atmosphere and Dust Environment Explorer mission. These anisotropies may also be observable through the analysis of pickup ions originating from the lunar exosphere [*Sarantos et al.*, 2012a], of which several spacecraft have recently reported measurements including Kaguya [*Yokota et al.*, 2009, 2014], Chang'E-1 [*Wang et al.*, 2011], and ARTEMIS [*Halekas et al.*, 2012, 2013a].

A deeper understanding of the microphysics involved in the reflection of solar wind ions by lunar crustal magnetic anomalies is critical to addressing the uncertainties in our calculations. While observations by Kaguya and Chandrayaan [*Lue et al.*, 2011; *Saito et al.*, 2012] have demonstrated that bulk reflection of the solar wind occurs over anomalies and recent modeling has begun to elucidate the physics deep within the anomaly region, there are many open questions, including the degree of particle heating and the role of nonadiabatic magnetic scattering. These questions must be fully explored before we completely understand the coupling between the solar wind, crustal anomalies, and the lunar exosphere. We also note that the two example solar wind conditions presented in section 2 and the corresponding neutral distributions discussed in section 3 are not meant to be exhaustive. In fact, a wide variety of solar wind conditions have been measured at 1 AU, with velocities ranging from 250 to 700 km/s, alpha contents from 0 to ≈25%, and proton temperatures from 1 to 25 eV. Additionally, the location of the crustal fields across the lunar dayside will vary according to lunar phase, inducing variable structure in the pattern of solar wind sputtered fluxes. Such variability will be compounded with the existing heterogeneous distribution of elements in the lunar regolith between different lunar regions (i.e., highlands, low- and high-Ti mare, and KREEP [potassium, rare earth elements, and phosphorus]) [*Papike et al.*, 1982; *Wurz et al.*, 2007]. Accounting for both surface composition variability and anisotropies in sputtered fluxes in crustal anomaly regions may be critical when interpreting variability or structure in observations of neutral sputtered species around the Moon.

Acknowledgments
The authors gratefully acknowledge support from NASA's Lunar Atmospheric and Dust Environment Explorer (LADEE) Guest Investigator program, grants NNX13AO71G (A.R.P. and J.S.H.) and NNX13AO74G (M.S.). The authors also acknowledge support by NASA's Solar System Exploration Research Virtual Institute. This publication is SSERVI contribution SSERVI-2014-097. The Kaguya data used in this study are available upon request to the authors, while the Lunar Prospector data can be found in the NASA Planetary Data System (PDS).

The Editor thanks three anonymous reviewers for their assistance in evaluating this paper.

References

Bamford, R. A., et al. (2012), Minimagnetospheres above the lunar surface and the formation of lunar swirls, *Phys. Rev. Lett.*, *109*, 081101.

Barghouty, A. F., F. W. Meyer, P. R. Harris, and J. H. Adams Jr. (2011), Solar-wind protons and heavy ion sputtering of lunar surface materials, *Nuc. Instr. Meth. B*, *269*, 1310–1315.

Biersack, J. P., and W. Eckstein (1984), Sputtering studies with the Monte Carlo Program TRIM.SP, *Appl. Phys. A*, *34*, 73–94.

Cassidy, T. A., and R. E. Johnson (2005), Monte Carlo model of sputtering and other ejection processes within a regolith, *Icarus*, *176*, 499–507.

Deca, J., A. Divin, G. Lapenta, B. Lembège, S. Markidis, and M. Horányi (2014), Electromagnetic particle-in-cell simulations of the solar wind interaction with lunar magnetic anomalies, *Phys. Rev. Lett.*, *112*, 151102.

Futaana, Y., S. Machida, Y. Saito, A. Matsuoka, and H. Hayakama (2003), Moon-related nonthermal ions observed by Nozomi: Species, sources, and generation mechanisms, *J. Geophys. Res.*, *108*(A1), 1025, doi:10.1029/2002JA009366.

Futaana, Y., S. Barabash, M. Wieser, C. Lue, P. Wurz, A. Vorburger, A. Bhardwaj, and K. Asamura (2013), Remote energetic neutral atom imaging of electric potential over a lunar magnetic anomaly, *Geophys. Res. Lett.*, *40*, 262–266, doi:10.1002/grl.50135.

Halekas, J. S., R. J. Lillis, R. P. Lin, M. Manga, M. E. Purucker, and R. A. Carley (2010), How strong are lunar crustal magnetic fields at the surface?: Considerations from a reexamination of the electron reflectometry technique, *J. Geophys. Res.*, *115*, E03006, doi:10.1029/2009JE003516.

Halekas, J. S., A. R. Poppe, G. T. Delory, M. Sarantos, W. M. Farrell, V. Angelopoulos, and J. P. McFadden (2012), Lunar pickup ions observed by ARTEMIS: Spatial and temporal distribution and constraints on species and source locations, *J. Geophys. Res.*, *117*, E06006, doi:10.1029/2012JE004107.

Halekas, J. S., A. R. Poppe, G. T. Delory, M. Sarantos, and J. P. McFadden (2013a), Using ARTEMIS pickup ion observations to place constraints on the lunar atmosphere, *J. Geophys. Res. Planets*, *118*, 81–88, doi:10.1029/2012JE004292.

Halekas, J. S., A. R. Poppe, J. P. McFadden, and K.-H. Glassmeier (2013b), The effects of reflected protons on the plasma environment of the Moon for parallel interplanetary magnetic fields, *Geophys. Res. Lett.*, *40*, 4544–4548, doi:10.1002/grl.50892.

Husinsky, W., I. Girgis, and G. Betz (1985), Doppler shift laser fluorescence spectroscopy of sputtered and evaporated atoms under Ar^+ bombardment, *J. Vac. Sci. Technol., B*, *3*(5), 1543–1545.

Jarvinen, R., M. Alho, E. Kallio, P. Wurz, S. Barabash, and Y. Futaana (2014), On vertical electric fields at lunar magnetic anomalies, *Geophys. Res. Lett.*, *41*, 2243–2249, doi:10.1002/2014GL059788.

Johnson, R. E., and R. Baragiola (1991), Lunar surface: Sputtering and secondary ion mass spectrometry, *Geophys. Res. Lett.*, *18*(11), 2169–2172.

Lue, C., Y. Futaana, S. Barabash, M. Wieser, M. Holmström, A. Bhardwaj, M. B. Dhanya, and P. Wurz (2011), Strong influence of lunar crustal fields on the solar wind flow, *Geophys. Res. Lett.*, *38*, L03202, doi:10.1029/2010GL046215.

Meyer, F. W., P. R. Harris, C. N. Taylor, H. M. Meyer III, A. F. Barghouty, and J. H. Adams (2011), Sputtering of lunar regolith simulant by protons and singly and multicharged Ar ions at solar wind energies, *Nuc. Instr. Meth. B*, *269*, 1316–1320.

Mitchell, D. L., J. S. Halekas, R. P. Lin, S. Frey, L. L. Hood, M. H. Acuña, and A. Binder (2008), Global mapping of lunar crustal magnetic fields by Lunar Prospector, *Icarus*, *194*, 401–409.

Papike, J. J., S. B. Simon, and J. C. Laul (1982), The lunar regolith: Chemistry, mineralogy, and petrology, *Rev. Geophys. Space Phys.*, *20*(4), 761–826.

Poppe, A. R., J. S. Halekas, G. T. Delory, and W. M. Farrell (2012), Particle-in-cell simulations of the solar wind interactions with lunar crustal magnetic anomalies: Magnetic cusp regions, *J. Geophys. Res.*, *117*, A09105, doi:10.1029/2012JA017844.

Saito, Y., et al. (2008), Solar wind proton reflection at the lunar surface: Low energy ion measurement by MAP-PACE onboard SELENE (KAGUYA), *Geophys. Res. Lett.*, *35*, L24205, doi:10.1029/2008GL036077.

Saito, Y., et al. (2012), Simultaneous observation of the electron acceleration and ion deceleration over lunar magnetic anomalies, *Earth Planets Space*, *64*, 83–92.

Sarantos, M., R. E. Hartle, R. M. Killen, Y. Saito, J. A. Slavin, and A. Glocer (2012a), Flux estimates of ions from the lunar exosphere, *Geophys. Res. Lett.*, *39*, L13101, doi:10.1029/2012GL052001.

Sarantos, M., R. M. Killen, D. A. Glenar, M. Benna, and T. J. Stubbs (2012b), Metallic species, oxygen and silicon in the lunar exosphere: Upper limits and prospects for LADEE measurements, *J. Geophys. Res.*, *117*, A03103, doi:10.1029/2011JA017044.

Schaufelberger, A., et al. (2011), Scattering function for energetic neutral hydrogen atoms off the lunar surface, *Geophys. Res. Lett.*, *38*, L22202, doi:10.1029/2011GL049362.

Sigmund, P. (1969), Theory of sputtering. I. Sputtering yield of amorphous and polycrystalline targets, *Phys. Rev.*, *184*, 383–416.

Thompson, M. W., B. W. Farmery, and P. A. Newson (1968), A mechanical spectrometer for analyzing the energy distribution of sputtered atoms of copper and gold, *Philos. Mag.*, *18*(152), 361–383.

Vorburger, A., P. Wurz, S. Barabash, M. Wieser, Y. Futaana, M. Holmström, A. Bhardwaj, and K. Asamura (2012), Energetic neutral atom observations of magnetic anomalies on the lunar surface, *J. Geophys. Res.*, *117*, A07208, doi:10.1029/2012JA017553.

Vorburger, A., P. Wurz, S. Barabash, M. Wieser, Y. Futaana, M. Holmström, A. Bhardwaj, and K. Asamura (2014), First direct observation of sputtered lunar oxygen, *J. Geophys. Res. Space Physics*, *119*, 709–722, doi:10.1002/2013JA019207.

Wang, X., M. Horányi, and S. Robertson (2012), Characteristics of a plasma sheath in a magnetic dipole field: Implications to the solar wind interaction with the lunar magnetic anomalies, *J. Geophys. Res.*, *117*, A06226, doi:10.1029/2012JA017635.

Wang, X., C. T. Howes, M. Horányi, and S. Robertson (2013), Electric potentials in magnetic dipole fields normal and oblique to a surface in plasma: Understanding the solar wind interaction with lunar magnetic anomalies, *Geophys. Res. Lett.*, *40*, 1686–1690, doi:10.1002/grl.50367.

Wang, X.-D., et al. (2010), Acceleration of scattered solar wind protons at the polar terminator of the Moon: Results from Chang'E-1/SWIDs, *Geophys. Res. Lett.*, *37*, L07203, doi:10.1029/2010GL042891.

Wang, X.-D., et al. (2011), Detection of m/q = 2 pickup ions in the plasma environment of the Moon: The trace of exospheric H_2^+, *Geophys. Res. Lett.*, *38*, L14204, doi:10.1029/2011GL047488.

Wieser, M., et al. (2009), Extremely high reflection of solar wind protons as neutral hydrogen atoms from regolith in space, *Planet. Space Sci.*, *57*, 2132–2134.

Wieser, M., et al. (2010), First observation of a mini-magnetosphere above a lunar magnetic anomaly using energetic neutral atoms, *Geophys. Res. Lett.*, *37*, L05103, doi:10.1029/2009GL041721.

Wurz, P., U. Rohner, J. A. Whitby, C. Kolb, H. Lammer, P. Dobnikar, and J. A. Martín-Fernández (2007), The lunar exosphere: The sputtering contribution, *Icarus*, *191*, 486–496.

Yokota, S., et al. (2009), First direct detection of ions originating from the Moon by MAP-PACE IMA onboard SELENE (KAGUYA), *Geophys. Res. Lett.*, *36*, L11201, doi:10.1029/2009GL038185.

Yokota, S., et al. (2014), Structure of the ionized lunar sodium and potassium exosphere: Dawn-dusk asymmetry, *J. Geophys. Res. Planets*, *119*, 798–809, doi:10.1002/2013JE004529.